Considerations on the Development of an Electric Drive for a Secondary Flight Control Electromechanical Actuator

Paolo Giangrande[1], Alessandro Galassini[1], Savvas Papadopoulos[1], Ahmed Al-Timimy[1], Giovanni Lo Calzo[1], Michele Degano[1], Michael Galea[1,2], Chris Gerada[1,2]

[1] Power Electronics, Machines and Control Group, University of Nottingham, Nottingham, UK,

[2] School of Aerospace, University of Nottingham Ningbo, Ningbo, China

p.giangrande@nottingham.ac.uk

Abstract – **The more electric aircraft concept aims to improve the fuel consumption, the weight and both the maintenance and operating costs of the aircraft, by promoting the use of electric power in actuation systems. According to this scenario, electromechanical actuators for flight control systems represent an important technology in next generation aircraft. The paper presents a linear geared electromechanical actuator for secondary flight control systems, where the safety and availability requirements are fulfilled by replicating the electric drive acting on the drivetrain. Indeed, the architecture considered consists of two power converters feeding as many electrical machines coupled to the same mechanical system. The design of both the permanent magnet synchronous machine and the power converter are addressed. Preliminary results on the electric drive prototype are also provided and compared to the design requirements. Finally, the electromechanical actuator performance at system-level is evaluated in Dymola environment, analyzing different operating modes.**

Index Terms – **DC-AC power converters, Electrohydraulics, Electromechanical systems, Fault tolerance, Permanent magnet machines, Redundancy.**

I. INTRODUCTION

In recent years, demanding regulations on fuel emissions and the need of decreasing both operating and maintenance costs have encouraged the aircraft industry to move from conventional hydraulic to electrical actuation systems [1-4]. This trend is supported by the inherent benefits offered by electrical actuation systems, such as a) weight reduction due to the removal of hydraulic pipelines, b) high dynamic performance ensured by both low inertia motors and high-bandwidth controllers and c) actuation distribution degree of freedom [5, 6].

Among the electrical actuation solutions, mainly two configurations can be identified, namely electro-hydrostatic actuators (EHAs) [7] and electromechanical actuators (EMAs) [8, 9]. In the former, electric power is used for supplying the electric drive, which is mechanically coupled to a hydraulic pump. Thus, hydraulic power is locally generated for driving the flight control surface. On the other hand, a mechanical drivetrain (e.g. gearbox and/or ball screw) is placed between the electric drive and the flight control surface [10], as schematically shown in Fig. 1.

Both EHAs and EMAs are currently employed on large commercial aircraft. In particular, the Boeing 787 uses EMAs for landing gear braking and spoiler surfaces [11, 12]. Similarly, the Airbus A380 adopts EHAs for ailerons and elevators (primary flight controls), while slats (secondary flight controls) are actuated by EMAs [13, 14]. The adoption of EHAs for the primary flight controls led to a 1500 kg weight reduction on the A380 [15]. Despite the local hydraulics and the higher maintenance costs [3], currently the use of EHAs is still more widely spread than EMAs, due to the well-established "know-how" regarding hydraulic systems [15, 16]. In fact, the risk of failures (e.g. jamming) and the lack of accumulated reliability experience [17] relegate EMAs to be currently implemented on secondary flight controls, such as flaps, spoilers and slats [11]. These controls are considered less safety-critical, due to the inherent surface redundancy of the aircraft wing, which is equipped with multiple surfaces performing the same aerodynamic task [18]. Nevertheless, EMAs represent an attractive technology, which is gaining interest due to its higher efficiency and further weight reduction compared to EHAs [1, 3, 19].
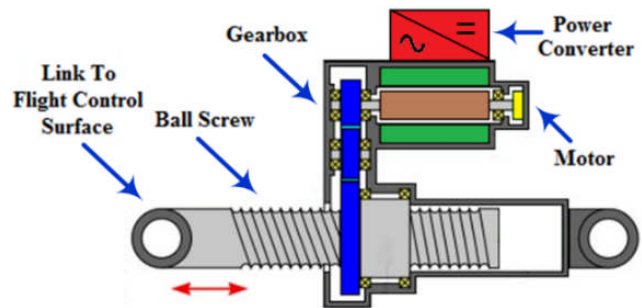
Fig. 1. Example of linear geared EMA.

A linear geared EMA for secondary flight control systems is considered in this work. Despite the existing surface redundancy of the aircraft wing, the EMA availability has been increased by duplicating the electric drive. Hence, two electrical machines powered by two isolated power electronics converters (PECs) and controlled by two Micro Controller Units (MCUs) are used for driving the EMA drivetrain. This architecture allows to achieve the safety requirements in case of a fault occurring in the electric drive components (i.e. MCUs, PECs and motors), which have a higher failure rate [8, 20]. The EMA failure probability is determined based on the

fault tree methodology [21, 22] and the value obtained for the described EMA electric drive configuration is compared against the ones regarding the existing technologies (i.e. EHA and purely hydraulic actuation system), in Section II.

In order to meet the challenging volume requirement, a permanent magnet synchronous machine (PMSM) is selected as the machine topology due to its high-power density and excellent efficiency [23, 24]. The PMSM design is discussed along with some manufacturing details and finite element (FE) analysis results. Details regarding the PEC design choices are given throughout the paper and its thermal management is evaluated by means of experimental tests. The electric drive performance is experimentally assessed and compared against the design outcomes. Since the EMA drivetrain (i.e. gearbox plus ball screw) is not yet available for fully integrated tests, the performance at system-level is simulated in Dymola environment, using purpose built models for the electric drive components [25, 26]. In particular, two EMA operating modes are investigated: 1) the active-active mode, where both electric drives are operated at the same time; and 2) the active-standby mode, where only one electric drive is powered (see Fig. 2).

II. ELECTRIC DRIVE DESIGN AND CONSIDERATIONS

In safety-critical applications, redundancy is often necessary for increasing the system availability. Despite the ever-growing importance gained by the electrical drives in modern aircraft, their components experience a higher failure rate compared to the mechanical drivetrain components [8]. Thus, a flexible "dual-branch" electric drive (i.e. redundant electric drive), acting on the same mechanical system, has been adopted for the considered EMA. The chosen fault-tolerant architecture is depicted in Fig. 2 and its failure probability is evaluated in the sub-section II.A.
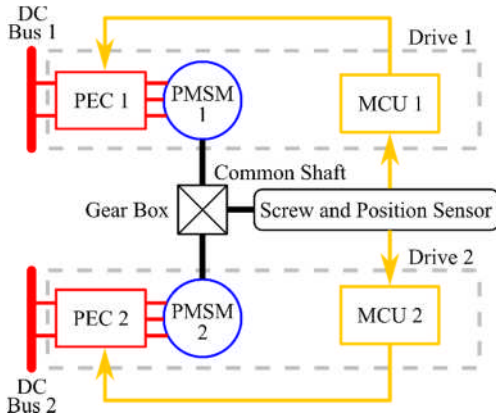
Fig. 2. Architecture of the considered EMA.

The two electric drives highlighted in Fig. 2 consist of an aluminium encased electrical drive and one PMSM each. The box of each drive encloses one MCU and one two-level custom inverter (i.e. PEC) fed by a 270 V DC bus. The linear geared EMA drivetrain is characterized by two stages: 1) the gearbox, which enhances the torque produced by both PMSMs and 2)

the ball screw, which converts the rotational motion of the gearbox output shaft in linear motion of the EMA rod-end. The gearbox features a 200:1 step-down ratio, while the ball screw's transmission ratio is equal to 500 rad/m. The next sub-subsections deal with the design and testing of both the PMSM and PEC, along with the EMA failure probability.

A. Failure probability of the EMA

On a civil airliner, the flight control systems actuated by a purely hydraulic system feature a failure probability of less than 10^{-9} per flight hour [21], which represents the target value for the replacing technologies (i.e. EHA and EMA). Using the components' failure rates reported in [21, 22], the fault tree for both EHA and EMA in "single-branch" configuration can be built. A "single-branch" EHA is characterized by a failure probability of 1.98×10^{-4} per flight hour, whereas 1.61×10^{-4} per flight hour is the failure probability of a "single-branch" EMA [21, 27]. The obtained values reveal that the "single-branch" configurations cannot guarantee the failure probability demanded by the flight control system. For this reason, "dual-branch" solutions (i.e. redundant configurations) need to be employed to reduce the failure probability, despite the increment in weight and cost.
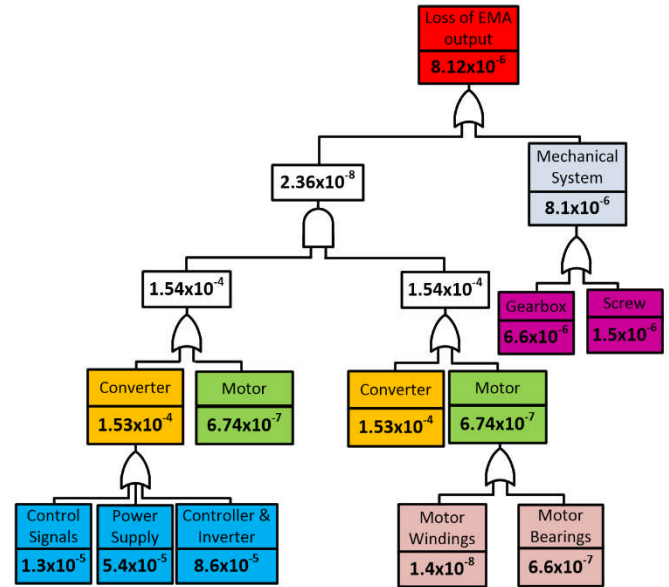
Fig. 3. Fault tree of the considered EMA.

The fault tree for the EMA architecture of Fig. 2 is shown in Fig. 3, where it can be observed that total failure probability is 8.12×10^{-6} per flight hour. From this diagram, it can be noted that the EMA's failure probability is constrained by the mechanical system, since its failure probability (i.e. 8.1×10^{-6}) results higher than the one of the "dual-branch" electric drive (i.e. 2.36×10^{-8}). While the EMA's failure probability does not meet the required value, it is still acceptable for the application at hand due to the inherent redundancy of the aircraft wing. Indeed, the presented EMA will only act on a single flight control surface.

B. PMSM Prototype: Design and Testing

For the application under study, each PMSM is required to deliver 5 Nm at 8000 rpm and operate at a maximum ambient temperature of 70 °C using natural air cooling system. Furthermore, to comply with the fast-dynamic response requirements, the moment of inertia should not exceed $10\text{-}4 \text{ kg} \cdot \text{m}^2$. According to these specifications and taking into account the limited available space (i.e. axial length ≤ 80 mm and outer diameter ≤ 80 mm), the design has been performed via FE analysis. A preliminary trade-off study has been carried out for selecting the appropriate slots/poles combination. In order to minimize both the torque ripple and the cogging torque, which might result in undesired effects on the EMA drivetrain, 9 slots / 8 poles machine configuration has been chosen [28]. Since distinguished by high fill-factor and short end-windings, a double-layer concentrated winding has been adopted, as shown in Fig. 4. This winding configuration contributes to lower copper losses [29], whereby the heat dissipation is facilitated. High permeability cobalt-iron alloy laminations have been used for the stator core, because they feature relatively high saturation flux density (i.e. 2.3 T) and lower specific iron losses if compared to silicon steel alloys.
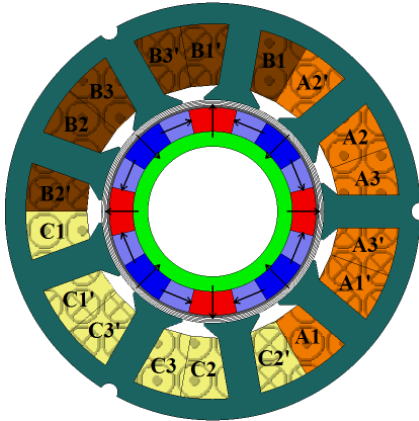
Fig. 4. Cross-section of the 9 slots / 8 poles PMSM.

In terms of permanent magnets (PMs) material, samarium-cobalt has been preferred to neodymium-iron-boron, due to the higher operating temperature capability. To increase the torque and reduce the back-electromotive force (back-EMF) harmonic content, the PMs on the rotor surface have been mounted in a quasi-Halbach array layout [30]. Despite higher cost and manufacturing complexity, the adoption of the quasi-Halbach array configuration leads to shorter axial length, which is beneficial for both the total PMSM mass and rotor inertia reduction. The PMs' eddy currents losses have been reduced by axially segmenting the PMs in 10 sectors, thus shortening the eddy currents paths through the PMs. This approach decreases the PMs' eddy currents losses by 43% at rated speed compared to when whole PMs (i.e. single segment) are used, hence it leads to a PMSM efficiency improvement. Since the PMs are mechanically brittle, a titanium retaining sleeve has

been used for holding the PMs on the shaft and protecting them during the PMSM assembling stage. For securing fast acceleration and containing the rotor inertia, a hollow shaft has been manufactured [31]. A magnetically permeable material (i.e. 17-4 PH stainless steel) has been selected for the shaft, in order to serve also as rotor back-iron. Finally, an aluminum housing equipped with radial fins has been designed for enhancing the heat dissipation by natural convection. In Fig. 5, the assembled PMSM prototype is depicted, whereas Table I summarises its parameters. The designed PMSM is characterized by an overall weight of 2.52 kg and its losses at rated operating condition are provided in Table II.

TABLE I
PMSM PROTOTYPE PARAMETERS

Parameter	Symbol	Value
Rated Speed	Ω_N	8000 rpm
Rated Torque	T_N	5 Nm
Rated Current	I_N	37.5 A_{pk}
Phase Resistance	r_s	175 mΩ
d-axis Inductance	L_d	0.276 mH
q-axis Inductance	L_q	0.276 mH
PM Flux	Ψ_{PM}	0.022 Wb
Stack Length	L	80 mm
Stator Outer Diameter	D_{out}	70 mm
Airgap Thickness	g	0.9 mm
Sleeve Thickness	S_{tk}	0.4 mm
Moment of Inertia	J	$10^{-4} \text{ kg} \cdot \text{m}^2$
Total Mass	M	2.52 kg

Fig. 5. Assembled PMSM prototype.

TABLE II
PMSM LOSSES AT RATED OPERATING CONDITION

Losses Term	Losses Value
Windings Losses	370 W
Stator Core Losses	42.3 W
Permanent Magnets Losses	41.8 W
Sleeve Losses	41.1 W
Shaft Losses	35.1 W
Total Losses	530.3 W

Preliminary tests have been performed under no-load and loaded conditions on the PMSM prototype for validating the FE design. The flux density map and the flux lines distribution at rated speed have been determined via FE simulations and the results are presented in Fig. 6. A comparison between experimental and FE back-EMFs at rated speed is proposed in Fig. 7, which reveals the back-EMFs low harmonic content resulting from the implementation of the quasi-Halbach array

configuration. In Fig. 7, the slight mismatch in amplitude is observable between experimental and FE waveforms. This is due to the end-effect caused by the permeable rotor endcaps, which leads to an increase of leakage flux [32]. The end-effect is not considered in 2D FE simulations, resulting in a higher back-EMF amplitude. Based on the FE results, the voltage constant is equal 11.5 mVrms/rpm, whilst 10.8 mVrms/rpm are obtained from the measurements (i.e. 6 % difference).
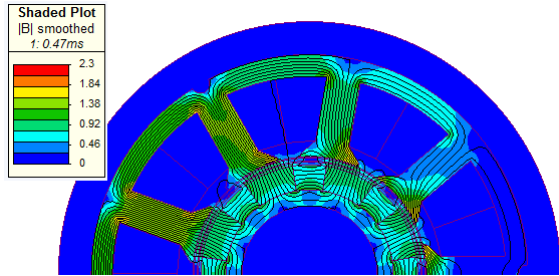
Fig. 6. No-load flux density map and flux lines distribution at 8000 rpm.
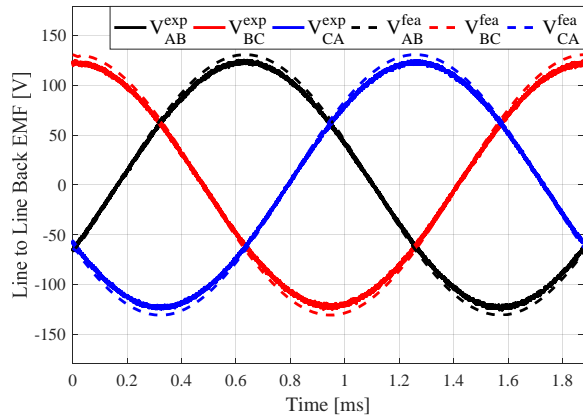
Fig. 7. Comparison between experimental (solid line) and FE (dash line) line-to-line back-EMFs at 8000 rpm.
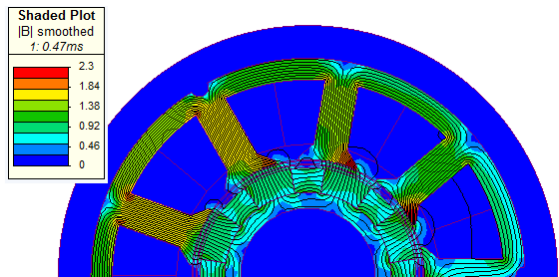
Fig. 8. Flux density map and flux lines distribution at 37.5 A and 8000 rpm.
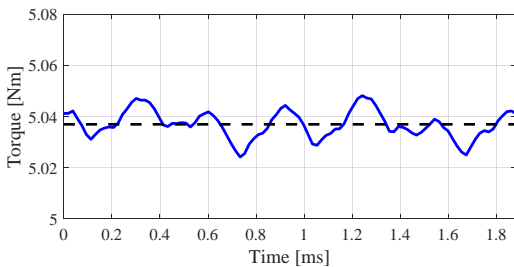
Fig. 9. Instantaneous torque at 37.5 Apk and 8000 rpm.

In order to develop the rated torque, the PMSM must be supplied with 37.5 A_{pk} (i.e. active-standby operating mode). The flux density map and the flux lines distribution at full load condition are shown in Fig. 8, from where can be seen that the saturation limit (i.e. 2.3 T) is reached only in the tooth-shoe area. In Fig. 9, the FE instantaneous torque is reported, presenting an average value of 5.037 Nm at rated current, whereas its torque ripple is equal to 0.22 %. The PMSM torque-current characteristic has been computed by FE simulations and further experimentally validated. The comparison is shown in Fig. 10, where a good agreement between measurements and FE is highlighted. According to the FE findings, the PMSM torque constant is equal to 0.134 Nm/A, while a torque constant of 0.129 Nm/A is calculated based on experimental data (i.e. 3.7 % mismatch).
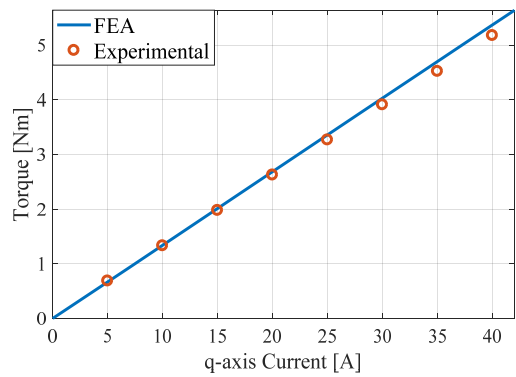
Fig. 10. Instantaneous torque Vs q-axis current characteristic: experimental (red dots) and FE (blue solid line).

Finally, a thermal analysis has been carried out on the PMSM [33, 34]. Considering the rated operating condition (i.e. 5 Nm at 8000 rpm) and an ambient temperature of 70 °C, the steady-state temperatures of the main PMSM components are as given in Table III.

TABLE III
PMSM TEMPERATURE DISTRIBUTION AT RATED OPERATING CONDITION

Component	Temperature
Windings	154.7 °C
Stator Core	136.4 °C
Permanent Magnets	129.9 °C

C. MCU and PEC Prototypes: Design and Testing

The MCU and PEC designs have considered various constraints and design specifications. The total volume, weight, maximum and minimum operating temperatures, and the cooling requirements are found to be the most challenging to achieve. Furthermore, the galvanic isolation between MCU, PEC, and the auxiliary power supplies had to be taken into account. Isolation between the MCU and the PEC is provided by the use of fibre optics and current sensors with galvanic isolation between the primary circuit (PEC) and the secondary side (MCU). Similar to the machine design, air cooling has been considered albeit with forced cooling. The design has been completed aiming to minimize the impact on the overall

weight. Four fans together with a Fabfin® high performance heatsink have been chosen for cooling the PEC unit.
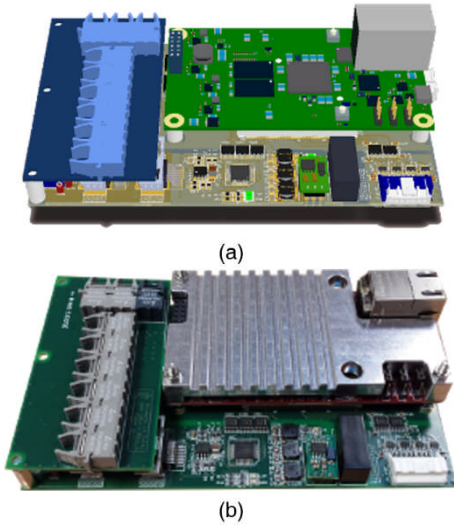
Fig. 11. View of the MCU: (a) Altium 3D without heat sink and (b) prototype with heatsink.
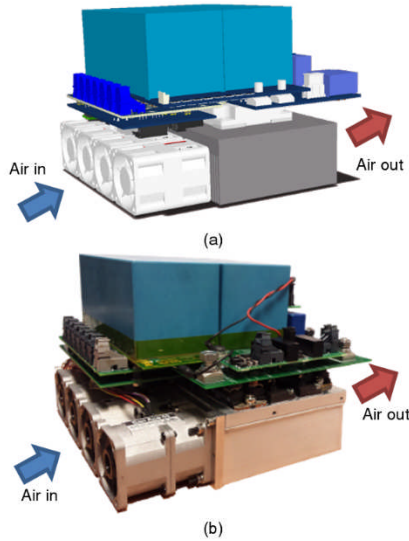
Fig. 12. View of the PEC: (a) Altium 3D and (b) prototype.

Only Silicon semiconductor technology has been considered over Wide Bandgap Devices (WBG) as its reliability and failure rates have been thoroughly investigated. An Infineon three-phase IGBT power module (FS100R07N3E4) with a two-level voltage source inverter and an embedded temperature sensor (NTC-thermistor) has been identified as a good solution for the power stage, both in terms of current ($I_{Cnom} = 100A$) and voltage ($V_{CES} = 650V$) ratings as well as minimization of semiconductor losses for the required switching frequency. All auxiliary systems are powered from a 28V DC bus. Considering an insulation of $3000V_{PK}$ between the auxiliary voltage (28V) and the DC bus (270V), the isolated DC-DC converters from Traco power (TMR3-2413HI) have been selected for suppling the gate drivers. For driving the IGBTs, the ACPL-339J Integrated Circuits (ICs), which provide for $5000V_{PK}$ voltage insulation,

an extended operating temperature range (-40 °C to 105 °C), and desaturation protection with soft turn-off, have been selected. Due to the high current required by the gate driver circuit, the ACPL-339J has been cascaded by a mosfet based current buffer. The MCU in Fig. 11 has been designed starting from the uCube [35] design, which is based on the Zynq-7000 System on Chip (SoC) from Xilinx. Phase currents and DC link voltage measurements can be sampled and filtered at 50 MHz using the Programmable Logic (PL) present within the SoC. Provided that the maximum fundamental electrical frequency (f_e) is 533.3 Hz, the switching and the interrupt frequency (f_{sw}) have been selected at 16 kHz. In order to enclose both the MCU and the PEC shown in Fig. 12, within the aluminum box in Fig. 13, the DC-link capacitor has been sized with the formula given in (1) to ensure minimal DC voltage ripple, where all the parameters are defined in Table IV.

$$C = \frac{\sqrt{3}\left(1 - \frac{V_{LL}^{PK}}{V_{DC}}\right)\frac{V_{LL}^{PK}}{V_{DC}}I_{OUT}^{RMS}}{\sqrt{2}f_{sw}\Delta V_{DC}^{PP}} \ [F] \qquad (1)$$

TABLE IV
DC-LINK CAPACITOR SIZING DATA

Symbol	Description	Value
I_{OUT}^{RMS}	Output RMS current	70A
V_{DC}	DC-Link voltage	270V
V_{LL}^{PK}	Line to line peak voltage	215V
ΔV_{DC}^{PP}	Peak to peak DC-link voltage ripple	1.35V
$f_{sw} \ or \ f_s$	Switching or interrupt frequency	16kHz
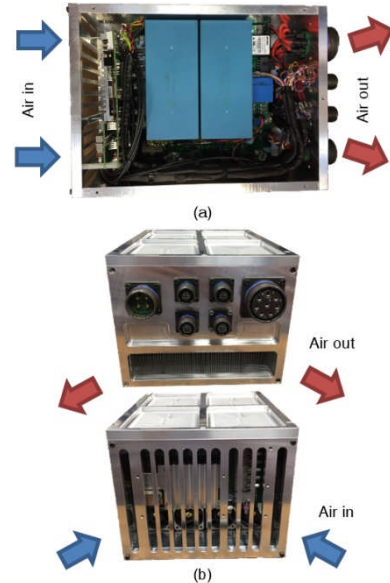
Fig. 13. Aluminum box enclosing both MCU and PEC: (a) Top view without lid and (b) side views.

Using (1), a capacitance of 643 µF is calculated. As the volume constraints have been met, a capacitance of 960 µF has been installed, paralleling two off-the-shelf capacitors from

EPCOS (B32778J4487K000). The overall weight of the designed PEC is equal to 7.61 kg.

The heat paths are highlighted in Figs. 12 and 13. In Fig. 14, temperatures profiles of the NTC, PEC heatsink, air in, and air out, while controlling a current of 44 ARMS on a dummy load, are shown respectively. Also assuming the worst-case ambient temperature (i.e. 70 °C), the IGBT power module works well within its temperature range, considering a maximum operating temperature equal to 150 °C. The results presented in Fig. 14 prove the effectiveness of the implemented cooling system.
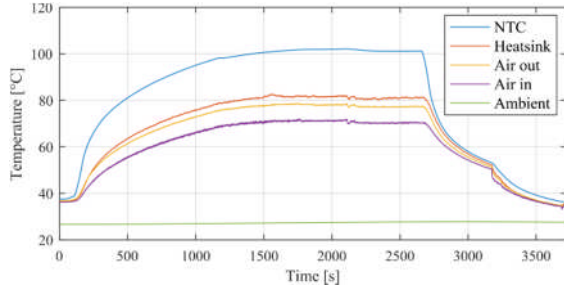
Fig. 14. Temperature profiles controlling $44A_{RMS}$ on a dummy load.

III. ELECTRIC DRIVE DESIGN AND CONSIDERATIONS

Following the design of the PMSM and the PEC, in order to assess the electric drive performance, a suite of integrated system tests have been conducted, where the PMSM is controlled in torque mode. Firstly, dq-current Proportional Integral (PI) controllers have been designed on the phase resistance r_s and on the transformed inductances L_d and L_q reported in Table I. In Fig. 15, the simplified current loop (modelling both actuation and current measurement delay), used for designing the PI dq-current controllers, is shown.
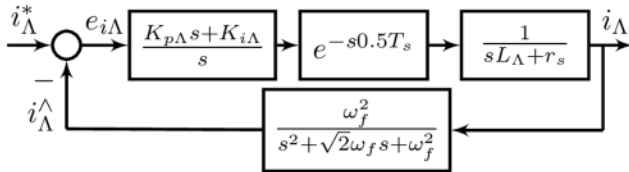
Fig. 15. Current loop within the reference frame with actuation and filtering delays. Λ represents either d- or q-axis, while the axes de-coupling is omitted.

TABLE V
INPUT DESIGN AND CONTROLLER PARAMETERS

Symbol	Description	Value
f_e	Fundamental electric frequency	533.3 Hz
T_s	Interrupt period	62.5 μs
f_f	Current filter cut-off frequency	200 kHz
ω_c	Current cross-over pulsation	11200 rad/s
φ_c	Current closed loop phase margin	80 deg
$K_{p\Lambda}$	Current loop proportional gain	2.4
$K_{i\Lambda}$	Current loop integral gain	8000

Since the PMSM presents no-saliency, the same proportional and integral parameters have been adopted in both the regulators. For simplicity, axis de-coupling has been omitted. In Fig. 15, where Λ represents either d or q, the actuation delay is taken into account by the pure delay $e^{-s0.5T_s}$, where $T_s = 1/f_{sw}$ is the interrupt period, whilst, the measurement delay is shaped as a second order low-pass filter with cut-off pulsation $\omega_f = 2\pi f_f$. In Table V, the parameters used for computing both the proportional $K_{p\Lambda}$ and the integral $K_{i\Lambda}$ gains, by imposing bandwidth ω_c and phase margin φ_c, are summarized [36, 37].
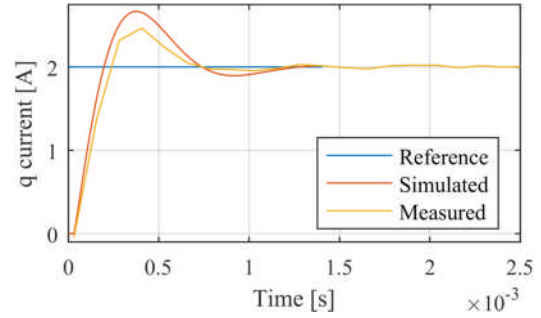
Fig. 16. Output q-current comparison at locked rotor.

In Fig. 16, the measured output current providing a q-current reference step of 2 A with locked rotor is compared against the output current from control diagram in Fig. 15. Sampled measurements and derived variables are saved and downloaded on the computer using a custom embedded scope coded within the MCU as shown in Fig. 11(b). Looking at the comparison, the simplified control diagram in Fig. 15 is accurate enough for designing the current PI regulators.

Fig. 17. Commercial high-speed interior permanent magnet machine used for spinning the PMSM under test.

The drive prototype introduced in the Section II is validated by imposing a load with the nominal torque at nominal speed. This is equivalent to the overall power demanded by the gearbox during active-standby operation when one drive is not supplied (5 Nm, equal to 37.5 Apk at 8000 rpm). On the other hand, in active-active operating mode, the power demanded to each drive is halved: 2.5 Nm, corresponding to 18.75 Apk, at 8000 rpm. Both active-active and active-standby operating modes have been validated by controlling the torque while spinning the machine under test at 8000 rpm by utilizing an industrial drive connected to an off-the-shelf high-speed interior permanent magnet machine, shown in Fig. 17. In Fig. 18, the measured mechanical angle ϑ_m when spinning the PMSM at 8000 rpm is reported, along with the electrical angle ϑ_e. In Figs. 19 and 20, the measured phase currents acquired

by the embedded scope in both active-active and active-standby operating modes are presented. As the sampling frequency matches the switching frequency, the switching ripple is not accounted for, which can give the impression of a small asymmetry when operating at low loads as seen in Fig 19. This has been validated as no other indications of asymmetry have been observed mechanically or electrically.
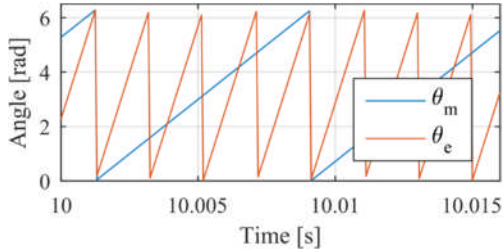
Fig. 18. Measured mechanical and electrical rotor position at 8000 rpm.
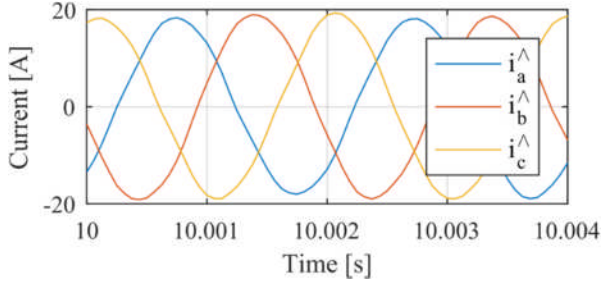
Fig. 19. Measured phase currents in active-active operating mode.
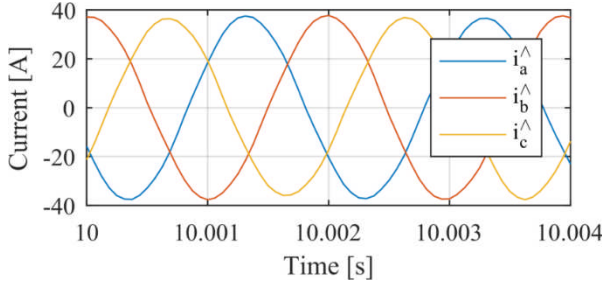
Fig. 20. Measured phase currents in active-standby operating mode.
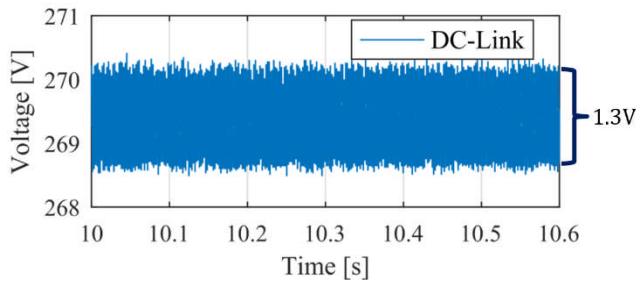
Fig. 21. DC-Link voltage in active-standby operating mode.

The PEC and the MCU enclosed in the box shown in Fig. 13 are able to control the PMSM current in both operating modes. Tests controlling the speed and the position will be performed pending on the availability of the mechanical drivetrain. In Fig. 21, the DC-Link voltage, during the active-standby operating mode, is shown. The measured maximum peak to peak DC-Link voltage ripple is equal to 1.3 V (i.e. 0.48%), which is smaller than the peak to peak DC-link voltage ripple

ΔV_{DC}^{PP} shown in Table IV and used in (1) for sizing the DC-Link capacitance. Considering the mission profile shown in the next section, the speed should be ramped from 0 rad/s to 837.75 rad/s (or 8000 rpm) in 0.429 s. This is equal to stepping from 0 rad/s to 100 rad/s in 51.25 ms. In Fig. 22, the measured rotor speed at no-load while providing a step input reference of 100 rad/s is depicted. Looking at the speed response and at the relative phase currents in Fig. 23, where the maximum absolute current is equal to 12 A, the drive shows the ability of reaching the full speed at no-load, starting from standstill.
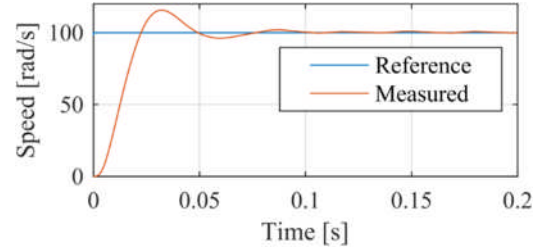
Fig. 22. Measured output speed providing a step reference of 100 rad/s (at no-load).
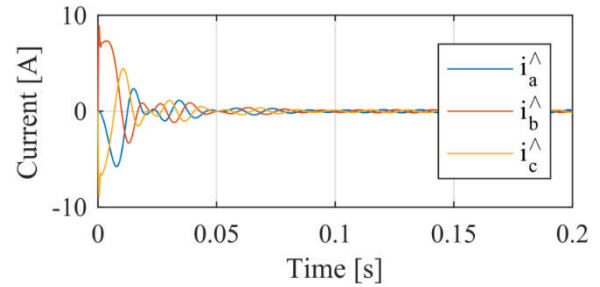
Fig. 23. Measured phase currents during speed transient of Fig. 21.

IV. EMA MISSION PROFILE

This final section of the paper dedicated to the full system performance evaluation. The fault-tolerant EMA architecture allows to perform the mission profile in two different operating modes: 1) active-active and 2) active-standby [38].
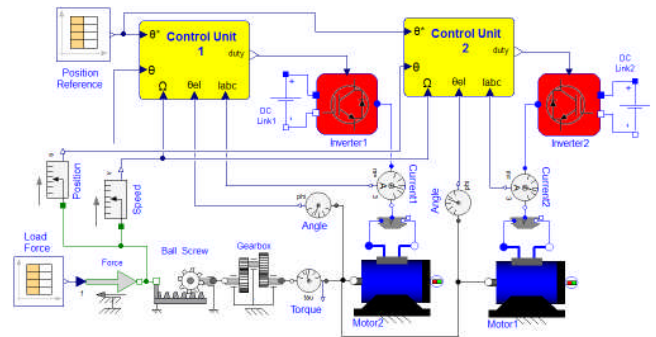
Fig. 24. EMA model in Dymola environment.

In the former operating mode, both PMSMs equally contribute to the EMA mission profile and each of them is supplied with half of the rated current (i.e. 18.75 A), generating 2.5 Nm. This operating mode is desirable, due to the lower current required for counteracting the load force. In fact, lower current results in lower copper losses, hence easier thermal management [39, 40]. In active-standby operating

mode, the EMA mission profile is solely performed by one PMSM, whereas the other is kept as a backup or it is intentionally de-energized in response to an electric fault detection [10]. In this condition, the active PMSM develops the rated torque by absorbing the rated current (i.e. 37.5 A). Hence, the PMSM copper losses are doubled compared to the active-active operating mode, thus, more heat needs to be dissipated.
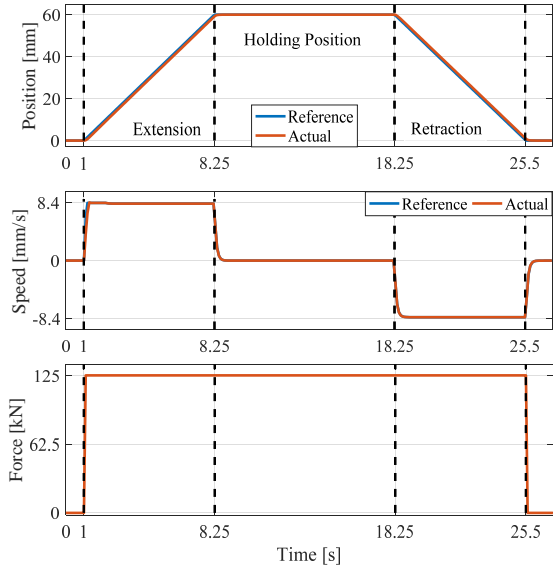
Fig. 25. EMA active-active mode: position (top sub-plot), speed (middle sub-plot), and load force (bottom sub-plot) of the end-rod.

Independently from the operating mode, the EMA mission profile consists in a full extension (60 mm stroke length covered in less than 7.5 s), followed by 10 s position holding and finally the rod-end travels back in the retracted position, whilst the load force is continuously applied. The rod-end position is tracked by a cascaded control structure. In particular, the inner loops control the *dq* current components of both PMSMs, while the outer loop regulates the rod-end speed. The outermost loop supervises the rod-end position. The model of the linear EMA has been implemented in Dymola environment using the Modelica language, as depicted in Fig. 24. Modelica is an object-oriented language, based on algebraic and ordinary differential equations [41]. The object-oriented approach is useful, since partial model and code can be reused. Additionally, the modelling environment provided by Dymola is ideal for multi-domain dynamic simulations, which are required for studying multidisciplinary systems, such as EMAs. Custom-made models have been used for the electric drive components [25, 26], whereas standard Dymola blocks have been adopted for the mechanical components.

The EMA is simulated in Dymola environment with the aim of qualitatively evaluating the performance at system-level. This choice was dictated by the unavailability of the mechanical drivetrain at the time of writing the paper. The

simulation results for the active-active operating mode are summarized in Fig. 25, where the mechanical quantities at the EMA end-rod are shown. The EMA exhibits suitable dynamic performance, although a modest position tracking error is present during both acceleration and deceleration periods (i.e. absolute tracking error of 0.83 mm corresponding to a percentage error equal to 0.63%). Similarly, active-standby simulation results configuration are reported in Fig. 26. Considering the mechanical quantities at the EMA end-rod, a satisfactory position tracking error is achieved along the whole trajectory; despite the saturation of the speed controller output, during the extension acceleration. Indeed, a moderate mismatch is observable between reference and actual speed signals at the end of the acceleration phase. The saturation of the speed controller output (occurring only during the extension acceleration) leads to a higher position tracking error compared to the previous operating mode (i.e. absolute tracking error of 1.25 mm corresponding to a percentage error equal to 2.08%).
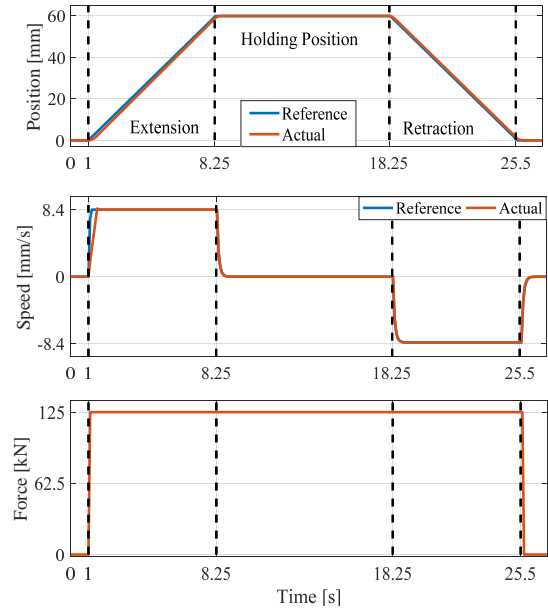
Fig. 26. EMA active-passive mode: position (top sub-plot), speed (middle sub-plot), and load force (bottom sub-plot) of the end-rod.

V. CONCLUSIONS

In this paper, the design and testing of an electric drive for aerospace EMA have been presented. The EMA was designed for secondary flight control systems and its availability was improved by adopting a redundant electric drive, which avoids single point of failure. Indeed, this solution allows to normally operate the EMA in active-active mode and move to active-standby mode, when an electric fault is detected on one electric drive. The PMSM performance has been evaluated via FE analysis and further compared against the experimental back-EMF waveforms and torque-current characteristic. The main outcome of the comparison is the influence of the permeable rotor endcaps, which leads to 6% and 3.7%

reduction on the induced back-EMF and on the developed torque, respectively. Nevertheless, the PMSM performance is still in line with the design specifications.

The design of the PEC was discussed and details regarding the MCU were provided. The PEC thermal management was experimentally tested and the obtained results proved its ability of safely operating also in the worst-case ambient temperature condition (i.e. 70 °C). Electric drive integration tests were performed and the obtained results were outlined and discussed. In particular, both current and speed step responses of the electric drive were assessed and the fine-tuning of the controllers was accomplished. By mechanically coupling the designed electric drive to a commercial one, the feasibility of working in active-active and active-standby modes has been demonstrated. Further experimental tests are scheduled on the EMA once its drivetrain will be available for the next step of the integration process. Finally, The EMA behavior was simulated in Dymola environment, considering the active-active and active-standby operating modes. Dymola results highlighted the EMA attitude of performing the required mission profile in all the simulated conditions.

REFERENCES

[1] I. Moir, A. Seabridge, and M. Jukes, "Electrical Systems," in *Civil Avionics Systems 2nd Edition, ISBN: 978-1-118-34180-3*, ed: John Wiley & Sons, 2013, pp. 235-290.

[2] P. Wheeler and S. Bozhko, "The More Electric Aircraft: Technology and challenges," in *IEEE Electrification Magazine*, vol. 2, n. 4, Dec. 2014.

[3] G. Qiao, G. Liu, Z. Shi, Y. Wang, S. Ma, and T.C. Lim, "A review of electromechanical actuators for More/All Electric aircraft systems," in *Proceedings of the Institution of Mechanical Engineers, Part C:Journal of Mechanical Engineering Science*, Nov. 2017.

[4] M. Lukic, A. Hebala, P. Giangrande, C. Klumpner, S. Nuzzo, G. Chen, C. Gerada, C. Eastwick, and M. Galea "State of the Art of Electric Taxiing Systems," in 2018 IEEE ESARS-ITEC, Nottingham UK, pp. 1-6, 2018.

[5] M. Villani, M. Tursini, G. Fabri, and L. Castellini, "Electromechanical actuator for helicopter rotor damper application," in *2012 XXth International Conference on Electrical Machines*, Sept. 2012.

[6] P. Giangrande, V. Madonna, G. Sala, A. Kladas, C. Gerada and M. Galea "Design and Testing of PMSM for Aerospace EMA Applications" in *44th Annual Conference of the IEEE Industrial Electronics Society*, pp. 1-6, Oct. 2018.

[7] G. Altare, A. Vacca and C. Richter, "A Novel Pump Design for an Efficient and Compact Electro-Hydraulic Actuator," in *2014 IEEE Aerospace Conference*, March 2014.

[8] J. W. Bennett, B. C. Mecrow, D. J. Atkinson, and G.J. Atkinson, "Safety-critical design of electromechanical actuation systems in commercial aircraft," in *IET EPA*, vol. 5, n. 1, pp. 37-47, Jan. 2011.

[9] C. Sciascera, P. Giangrande, C. Brunson, M. Galea, and C. Gerada, "Optimal design of an electro-mechanical actuator for aerospace application," in *41st Annual Conference of the IEEE Industrial Electronics Society*, pp. 1903-1908, Nov. 2015.

[10] V. Madonna, P. Giangrande, C. Gerada, and M. Galea., 2018, "Thermal analysis of fault-tolerant electrical machines for aerospace actuators," in press on *IET Electric Power Applications*. Available: http://digital-library.theiet.org/content/journals/10.1049/iet-epa.2018.5153.

[11] J.C. Derrien, "EMA advanced technologies for flight controls," in 28th International Congress of the Aeronautical Sciences, 2012.

[12] M. Sinnett, "Boeing: 787 No-Bleed Systems: Saving Fuel and Enhancing Operational Efficiencies," *AERO Quaterly QTR_04 07, 2007*.

[13] J. Fu, J. C. Mare and Y.L. Fu, "Modelling and simulation of flight control electromechanical actuators with special focus on model architecting, multidisciplinary effects and power flows," in *Chinese Journal of Aeronautic*, vol. 3, n. 1, pp. 47-65, Nov. 2016.

[14] M. Todeschi, "Airbus - EMAs for flight controls actuation system 2012 status and perspectives," in *Recent Advances in Aerospace Actuation Systems and Components*, Toulouse, France, 2012.

[15] M.A. Ismail, E. Balaban, and H. Spangenberg, "Fault Detection and Classification for Flight Control Electromechanical Actuators," in *2016 IEEE Aerospace Conference*, March 2016.

[16] P. Giangrande, V. Madonna, S. Nuzzo, and M. Galea, "Design of Fault-Tolerant Dual Three-Phase Winding PMSM for Helicopter Landing Gear EMA," in *Int. Conference on Electrical Systems for Aircraft, Railway, Ship Propulsion and Road Vehicles* (ESARS-ITEC), 2018.

[17] F. Cupertino, P. Giangrande, L. Salvatore, and G. Pellegrino, "Model based design of a sensorless control scheme for permanent magnet motors using signal injection," in *2010 IEEE Energy Conversion Congress and Exposition*, 2010, pp. 3139-3146.

[18] J. W. Bennett, B. C. Mecrow, D. J. Atkinson, C. Maxwell, and M. Benarous, "Fault-tolerant electric drive for an aircraft nose wheel steering actuator," in *IET EST*, vol. 1, n. 3, pp. 117-125, Oct. 2011.

[19] P. Giangrande, F. Cupertino and G. Pellegrino, "Modelling of linear motor end-effects for saliency based sensorless control," in 2010 IEEE Energy Conversion Congress and Exposition, pp. 3261-3268, 2010.

[20] J. Liscouet, M. Budinger, and J. C. Mare, "Design for Reliability of Electromechanical Actuators," in Recent Advances in Aerospace Actuation Systems and Components, Toulouse, France, 2010.

[21] J.W. Bennett "Fault Tolerant Electromechanical Actuators for Aircraft", PhD Thesis, Newcastle University, 2010.

[22] M. Rottach "Drive-System Optimization for a Helicopter Electromechanical Actuation System", PhD Thesis, Nottingham University, 2014.

[23] S.A. Odhano, P. Giangrande, R. Bojoi, and C. Gerada, "Self-commissioning of interior permanent magnet synchronous motor drives with high-frequency current injection," in 2013 Energy Conversion Congress and Exposition (ECCE), pp. 3852-3859, 2013.

[24] Z. Xu, A. Al-Timimy, M. Degano, P. Giangrande, G. Lo Calzo, H. Zhang, M. Galea, C. Gerada, S. Pickering, and L. Xia, "Thermal management of a permanent magnet motor for a directly coupled pump," in International Conference on Electrical Machines (ICEM), pp. 1-6, 2016.

[25] P. Giangrande, C.I. Hill, S.V. Bozhko, and C. Gerada, "A novel multi-level electro-mechanical actuator virtual testing and analysis tool," in *7th IET Conference on Power Electronics, Machines and Drives*, pp 1-6, April 2014.

[26] C.I. Hill, S.V. Bozhko, Y. Tao, P. Giangrande, and C. Gerada, "More Electric Aircraft Electro-Mechanical Actuator Regenerated Power Management," in *IEEE 24th International Symposium on Industrial Electronics*, pp 337-342, June 2015.

[27] Sadeghi, T. Lyons, A. "Fault Tolerant EHA Architectures", in *IEEE Aerospace and Electronic Systems Magazine*, Mar 1992 Volume: 7, Issue: 3, Part 1 pp.32-42.

[28] M. Galea, L. Papini, H. Zhang, C. Gerada, and T. Hamiti, "Demagnetization Analysis for Halbach Array Configurations in Electrical Machines," *IEEE Trans. on Magnetics*, vol. 51, n. 9, 2015.

[29] A. Al-Timimy, P. Giangrande, M. Degano, M. Galea, C. Gerada, "Investigation of AC Copper and Iron Losses in High-Speed High-Power Density PMSM", in Proc. 2018 XIII International Conference on Electrical Machines (ICEM), Alexandroupoli, Greece, 2018, pp. 263-269.

[30] C. Xia, L. Guo, H. Wang, "Modeling and analyzing of magnetic field of segmented Halbach array PM machine considering gap between segments," *in IEEE Trans. on Magnetics*, vol. 50, n. 12, Dec. 2014.

[31] A. Al-Timimy, P. Giangrande, M. Degano, M. Galea and C. Gerada, "Comparative study of permanent magnet-synchronous and permanent magnet-flux switching machines for high torque to inertia applications,"

in *2017 IEEE Workshop on Electrical Machines Design Control and Diagnosis (WEMDCD)*, pp 45-51, Nottingham, UK, April 2017.

[32] A. Al-Timimy, M. Alani, M. Degano, P. Giangrande, C. Gerada, and M. Galea, "Influence of Rotor Endcaps on the Electromagnetic Performance of High Speed PM Machine," in *IET Electric Power Applications*, vol. 12, n. 8, pp. 1142-1149, August 2018.

[33] C. Sciascera, M. Galea, P. Giangrande, and C. Gerada, "Lifetime consumption and degradation analysis of the winding insulation of electrical machines," in *8th IET International Conference on Power Electronics, Machines and Drives (PEMD 2016)*, 2016, pp. 1-5.

[34] A. Al-Timimy, G. Vakil, M. Degano, P. Giangrande, C. Gerada, and M. Galea, "Considerations on the Effects that Core Material Machining has on an Electrical Machine's Performance", in IEEE Transaction on Energy Conversion, vol. 33, no. 3, pp. 1154-1163, 2018.

[35] A. Galassini, G. Lo Calzo, A. Formentini, C. Gerada, P. Zanchetta and A. Costabeber, "uCube: Control platform for power electronics," *2017 IEEE Workshop on Electrical Machines Design, Control and Diagnosis (WEMDCD)*, Nottingham, 2017.

[36] R. De Doncker, D. Pulle, and A. Veltman, "*Advanced Electrical Drives: Analysis, Modeling, Control*", ser. Power Systems. Springer Netherlands, 2010.

[37] Z. Huang, T. Yang, P. Wheeler, M. Galea, P. Giangrande, and S. Chowdhury, "An active modulation scheme to boost voltage utilisation of the dual converter with a floating bridge," IEEE Transactions on Industrial Electronics, vol. 66, n. 7, pp. 5623-5633, July 2019.

[38] P. Giangrande, A. Al-Timimy, A. Galassini, S. Papadopoulos, M. Degano and M. Galea, "Design of PMSM for EMA Employed in Secondary Flight Control Systems," in 2018 IEEE ESARS-ITEC, Nottingham UK, pp. 1-6, 2018.

[39] V. Madonna, A. Walker, P. Giangrande, C. Gerada, G. Serra and M. Galea, "Improved thermal management and analysis for stator end-windings of electrical machines," IEEE Transactions on Industrial Electronics, vol. 66, n. 7, pp. 5057-5069, July 2019.

[40] V. Madonna, P. Giangrande, A. Walker, and M. Galea, "On the Effects of Advanced End-Winding Cooling on the Design and Performance of Electrical Machines," in *2018 XIII International Conference on Electrical Machines (ICEM)*, 2018, pp. 311-317.

[41] P. Fritzson, "Principles of object-oriented modeling and simulation with Modelica 2.1," IEEE Press, Piscataway, NJ, 2004.